Network-Level Performance Analysis for Air-Ground Integrated Sensing and Communication

Yihang Jiang, Xiaoyang Li, Guangxu Zhu, Kaifeng Han, Kaitao Meng, Chenji Liu, Wu Yang, Qingjiang Shi, and Rui Zhang

***Abstract*—To support the development of air-ground integrated sensing and communication (ISAC), network-level performance analysis is needed for providing an essential guide on the network design. Following the widely adopted orthogonal frequency-division multiplexing (OFDM) technology in existing wireless systems, a cooperative air-ground wireless network based on OFDM-ISAC is introduced in this paper, where the ISAC-enabled base stations (BSs) following the two-dimensional homogeneous Poisson point process (HPPP) distribution serve the terrestrial communication users while sensing the aerial targets. In particular, cooperative beamforming schemes are designed for mitigating the interference among ISAC BSs. First, we analyze the communication as well as sensing performances in terms of different metrics including area communication coverage probability, area communication spectral efficiency, area radar detection coverage probability, and average Cramér-Rao Bound. Simulation results are then presented to validate the theoretical analysis and illustrate the effects of key system parameters on the network performance. It is observed that both the communication and sensing (C&S) performances depend on the BS density and height, while the sensing performance also depends on the height of sensing target together with the numbers of OFDM subcarriers and symbols. Moreover, there exists tradeoffs between the C&S performances with respect to the BS density and height. The results of this paper provide useful guidance to the design and implementation of air-ground wireless network for harnessing the dual benefits of ISAC.**

***Index Terms*—Integrated sensing and communication, orthogonal frequency-division multiplexing, air-ground network analysis, stochastic geometry, beamforming.**

I. Introduction

As an innovative technological paradigm, integrated sensing and communication (ISAC) aims to unify the traditionally separate functions of sensing and wireless communication within a single system [1]. By leveraging shared resources such as spectrum, hardware, and signal processing techniques, ISAC seeks to enhance the efficiency and performance of both sensing and communication tasks [2]. As one of the key enabling technologies for the sixth generation (6G) wireless system, ISAC has attracted increasing research interest from both academia and industry in recent years [3]–[7]. However, most of the existing works in this area focus on single cell rather than the network-level ISAC systems [8], [9].

Y. Jiang, X. Li, G. Zhu, and Q. Shi are with the Shenzhen Research Institute of Big Data, The Chinese University of Hong Kong-Shenzhen, Guangdong, China. Q. Shi is also with Tongji University, Shanghai, China. K. Han is with China Academy of Information and Communication Technology, Beijing, China. K. Meng is with the Department of Electronic and Electrical Engineering, University College London, London, UK. C. Liu and W. Yang are with China Mobile Communications Group Jiangxi Co., Ltd, Jiangxi, China. R. Zhang is with The Chinese University of Hong Kong-Shenzhen, Guangdong, China, and also with the National University of Singapore. Corresponding author: X. Li (Email: lixiaoyang@sribd.cn).

Network-level performance analysis helps to gain insights that can guide the actual deployments of multi-cell wireless networks. As a powerful mathematical tool, stochastic geometry (SG) has been widely used in a series of communication network analysis [10]. In [11], the coverage probabilities and average rates for downlink communication scenarios are analyzed with the homogeneous Poisson point process (HPPP) distribution of base stations (BSs) and stationary point process distribution of communication users (CUs). However, as an initial exploration in this field, the analysis therein is limited to the single-antenna case, which restricts the ability to leverage the spatial gain provided by multiple antennas. In [12], the multiuser multiple-input multiple-output (MU-MIMO) in distributed antenna systems is considered for analyzing the per-CU throughput and area spectral efficiency, with the cooperative strategies among multiple distributed antennas in a typical cellular scenario. Following this work, the randomness of the BS and CU locations is further considered in [13], based on which the ergodic sum rate per-BS under different system parameters is derived. The analysis is further extended to the millimeter-wave (mmWave) scenarios [14].

In addition to performance analysis of communication networks, the sensing performance can also be analyzed via SG in radar and sensor networks. For example, the achievable detection probability in orthogonal frequency-division multiplexing (OFDM)-based radar networks is investigated in [15] by employing a Gaussian approximation of the aggregate interference. [16] makes a step forward by modeling and analyzing the statistical characteristics of radar interference in a linear automotive radar network under various vehicle spatial distribution models. In [17], the co-channel interference for automotive radar is analyzed using the SG tools.

Compared with communication-only and sensing-only networks, ISAC networks involve communication and sensing (C&S) interference. In [18], the effects of interference on ISAC performance are analyzed, where the time slots were divided for communication and sensing separately. As a further step, the effects of building blockage on the ISAC network performance are investigated in [19]. Taking simultaneous C&S into consideration, a mathematical framework is established in [20] to characterize the C&S coverage probability and the ergodic rate in an ISAC network. Moreover, the C&S performances are jointly considered in [21], where the sensing performance is evaluated via Cramér-Rao Bound (CRB). The beamforming (BF) design for ISAC network is considered in [22], based on which the spectrum efficiency and energy efficiency are analyzed. Following this line of

work, the cooperative ISAC is considered to mitigate sensing interference by applying a customized BF strategy [23]. In addition, the cooperative BS cluster sizes and the numbers of CUs/sensing targets (STs) are investigated to achieve a balanced performance tradeoff between C&S [24].

However, all the above studies focus exclusively on terrestrial CUs and STs, which might overlook the effects of altitude differences on aerial CUs or STs. With the rapid development of non-terrestrial networks and low-altitude economy, the CUs and STs are not only distributed on the ground but also in the low-altitude airspace [25]. To support air-ground C&S, the ISAC BSs are expected to be deployed in 6G networks [26], where the network performance remains to be analyzed. Moreover, as the OFDM waveform provides both excellent communication performance and sufficient flexibility for various sensing purposes, it is widely adopted in the design of ISAC networks [27].

In this paper, the network-level C&S performance in a cooperative air-ground OFDM-ISAC network is investigated using SG tools, where the ISAC BSs following a two-dimensional (2-D) HPPP distribution serve the terrestrial CUs while sensing the aerial STs. The cooperative BF schemes are designed for mitigating the sensing interference. The effects of system parameters on communication and sensing performances are further analyzed, including the BS density, BS height, ST height, as well as the number of OFDM subcarriers and transmission symbols. The main contributions of this paper are summarized as follows.

- *Air-ground OFDM-ISAC network framework:* As a new framework for 6G, the air-ground OFDM-ISAC network is introduced in this paper, where the ISAC BSs are deployed following the 2-D HPPP distribution to serve the terrestrial CUs while sensing the aerial STs. Compared with the conventional ISAC networks with terrestrial CUs and STs, additional parameters such as BS height and ST height are taken into consideration.
- *Cooperative BF strategies:* The BFs of adjacent BSs are collaboratively designed to mitigate the interference. A linear zero-forcing (ZF) BF strategy is designed at the transmitter and a maximum ratio combining (MRC) BF strategy is designed at the receiver. The cooperative BF strategies can effectively mitigate the interference between ISAC BSs.
- *C&S performance analysis:* The C&S performances are analyzed in terms of different metrics including area communication coverage probability (ACCP), area communication spectral efficiency (ACSE), area radar detection coverage probability (ARDCP) under the constant false alarm rate (CFAR) criterion, and average Cramér-Rao Bound (ACRB). For communication, the effects of system parameters including BS density and height on ACCP and ACSE are analyzed. The closed form of ACCP is further derived with the specific path loss exponent $\alpha_c = 4$. For sensing, the effects of system parameters such as the number of OFDM subcarriers and symbols on ARDPC and ACRB are analyzed. The closed form of the required radar SIR given a specific CFAR is further derived based on the strongest interferer approximation.
- *Guides on network deployment:* Simulations are conducted to validate the theoretical analysis and illustrate the effects of system parameters on the network performance. It is observed that increasing the BS height results in better sensing performance but worse communication performance, which indicates that there exists a tradeoff between C&S performances. Moreover, both the ACCP and ARDCP first increase and then decrease with the increasing BS density, while the maximum ACCP or ARDCP is achieved at different BS densities. The sensing performance can be further improved by increasing the numbers of OFDM subcarriers and symbols, or decreasing the ST height. These results serve as useful guides on the deployment of air-ground OFDM-ISAC networks for achieving balanced C&S performances.

The rest of the paper is organized as follows. The air-ground OFDM-ISAC network framework is introduced in Section II. The C&S performances in terms of different metrics are analyzed in Section III and Section IV, respectively. Section V and Section VI provide simulation results and conclusions, respectively.

Notations: In this paper, boldface letters refer to vectors (lower case) or matrices (upper case). For an $M \times N$ complex matrix $\mathbf{A} \in \mathbb{C}^{M\times N}$, $\mathbf{A}^T$, $\mathbf{A}^H$ and $\mathbf{A}_{[m,n]}$ denote its transposition, Hermitian and the entry in the m-th row and n-th column, respectively. $x!$, $\sum x$ and $\int x\, dx$ denote the factorial, sum and integral operations of x, respectively. For a random variable (RV) X, $\mathbb{E}\{X\}$, $\mathbb{E}\{X^2\}$, $\text{Var}\{X\} = \mathbb{E}\{X^2\} - \mathbb{E}^2\{X\}$ and $\mathbb{P}\{X > T\}$ denote its expectation, second-order moments, variance and the probability of event $X > T$, respectively. $X \sim \mathcal{CN}(\mu, \sigma^2)$, $X \sim \Gamma(\alpha, \beta)$ and $X \sim \text{Exp}(\lambda)$ represent the circularly symmetric complex Gaussian (CSCG), Gamma and exponential distributions of the RV X, respectively, where μ and σ^2 represent the mean and variance for the CSCG distribution, α and β are the shape and scale parameters for the Gamma distribution, and λ is the intensity parameter for the exponential distribution.

II. Networks Framework

A. ISAC Network Model

As shown in Fig. 1, a downlink ISAC network consisting of BSs, terrestrial CUs and aerial STs is considered, where each BS is equipped with a vertically placed half-wavelength uniform linear array (ULA) consisting of N_t antennas for transmitting ISAC signals and N_r antennas for receiving radar sensing echos. [1] The ISAC signals are used for serving single-antenna CUs and sensing the non-cooperative aerial STs simultaneously. [2] The locations of BSs are randomly distributed according to the 2-D HPPP with density λ_B BSs/Km^2, while CUs and STs are located according to independent stationary point processes. The heights of the BSs, CUs, and STs are h_B m, h_U m and h_T m above the ground, respectively.

[1] With the ULA placed vertically, the orientation of the BS does not affect the position of each antenna. The antenna radiation pattern of the BS is vertically directional and horizontally omnidirectional, which can be achieved by multi-sector antennas.

[2] It is assumed that the self-interference between the transmit and receive antennas is mitigated using electromagnetic shielding.

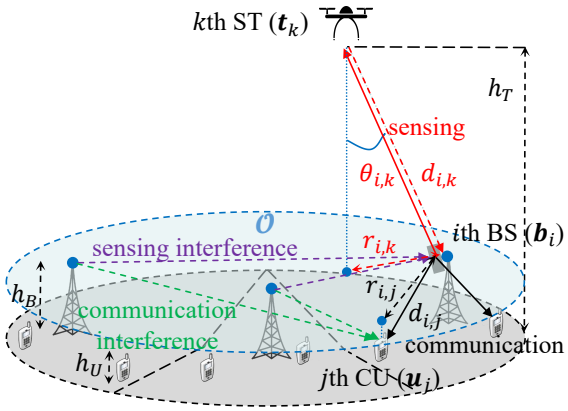

Figure 1: The ISAC network with low-altitude aerial sensing targets.

Without loss of generality, it is assumed that $h_T > h_B > h_U$ and each BS is required to serve multiple CUs and sense several STs under the nearest-neighbor association strategy.

Under the common SG analytical framework, we focus on the typical i-th BS, j-th CU and k-th ST to generally represent the average performance in the network [11]. By taking the horizontal plane $\mathcal{O}$ where BSs are located as the reference, the specific geometry model is illustrated in Fig. 1, where the locations of BS, CU and ST are denoted as $\boldsymbol{b}_i = (x_i, y_i, h_i)$, $\boldsymbol{u}_j = (x_j, y_j, h_j)$ and $\boldsymbol{t}_k = (x_k, y_k, h_k)$, respectively. Let $r_{i,j}$ and $r_{i,k}$ denote the horizontal ground distances from the BS to the CU and the ST, respectively. $\Delta h_c = h_B - h_U$ represents the vertical distance between the BS and the CU, while $\Delta h_r = h_T - h_B$ represents the vertical distance between the ST and the BS. The distances between the BS and the CU as well as the ST are given by $d_{i,j}$ and $d_{i,k}$, respectively. The angle of departure of ISAC signal as well as the angle of arrival of sensing echo signals are denoted by $\theta_{i,k} = \arccos\frac{\Delta h_r}{\|\boldsymbol{b}_i - \boldsymbol{t}_k\|_2} = \arcsin\frac{r_{i,k}}{\|\boldsymbol{b}_i - \boldsymbol{t}_k\|_2}$.

B. Signal Model

Benefiting from the excellent communication and sensing capabilities of OFDM signal, it is adopted in our considered ISAC network. Specifically, we assume that the ISAC system operates at the carrier frequency f_c over a total bandwidth B that is divided into N OFDM subcarriers with subcarrier spacing Δf. For an OFDM frame consisting of M OFDM symbols, each OFDM symbol duration can be denoted as $T = T_g + T_s$, where T_g and T_s denote the guard interval and data symbols duration, respectively, leading to a subcarrier spacing $\Delta f = \frac{1}{T_s}$. Focusing on an OFDM frame consisting of $M \times N$ time-frequency resource blocks, we consider that each serving BS communicates with J CUs within its cell, while simultaneously sensing K STs within the cell using dual-function ISAC signals during the coherent processing interval (CPI) [1]. Furthermore, the channel is assumed to be stationary over the entire time-frequency resource blocks.

1) Communication Model: To ensure fair distribution of interference among the CUs, each CU is assumed to be randomly allocated N/J subcarriers for data transmission. Consequently, following the literature [20], [28], [29], we focus on performance metrics defined for arbitrary resource elements in the context of communication. Without loss of generality, the serving BS is referred to as BS 1 and it is assumed that the J CUs served by this BS receive equal power allocation across all resource elements. Then, for arbitrary resource elements, the received communication signal at the typical CU can be expressed as [3]

$$y_c = \sqrt{P_t \mathcal{L}_1^c}\boldsymbol{h}_1^H \boldsymbol{x}_1 + \underbrace{\sum_{i \in \Phi_B | 1} \sqrt{P_t \mathcal{L}_i^c}\boldsymbol{h}_i^H \boldsymbol{x}_i}_{\text{inter-cell interference}} + z_1, \tag{1}$$

where P_t denotes the transmit power, $\mathcal{L}_i^c = \left(\frac{\lambda_c}{4\pi}\right)^2 d_i^{-\alpha_c}$ represents the pathloss for the communication channel with exponent α_c over a transmission distance d_i, λ_c is the wavelength of the carrier, $\boldsymbol{h}_i^H \in \mathbb{C}^{1\times N_t}$ denotes the communication channel vector between BS i and the typical CU, with every entry following $\mathcal{CN}(0,1)$, $\boldsymbol{x}_1 = \boldsymbol{w}_1 s_1$ denotes the unit-power intended signal for the typical CU precoded by the normalized BF vector $\boldsymbol{w}_1 \in \mathbb{C}^{N_t \times 1}$, $\boldsymbol{x}_i \in \mathbb{C}^{N_t \times 1}$ represents the transmitted signal from BS i that shares the same resource elements as the typical CU, and $z_1 \sim \mathcal{CN}(0, \sigma_c^2)$ is the addictive white Gaussian noise vector with variance σ_c^2. It is assumed that the symbols satisfy $|s_i| = 1$ due to constant-amplitude modulation, and thus the statistical properties of the reference signal and noise remain unchanged after element-wise division by the transmitted symbols.

2) Sensing Model: The sensing model is different from communication that focuses on data transmission during a particular resource element. Since ST-related parameter information is coupled in the time, frequency, and spatial domains, and radar's sensing capability is positively correlated with the number of accessible resources, radar sensing tends to utilize the echo signals from the entire resource blocks during the CPI. The line-of-sight (LoS) mono-static sensing is considered in our model. Specifically, the sensing tasks considered in this work include target detection and target parameter estimation. Since the angular information is coupled in the spatial domain and is not specific to OFDM waveforms, any conventional angle estimation algorithm (e.g., MUSIC [30]) can estimate the angular information. Therefore, in this work, the parameters of interest for the STs are the relative distance d_{rel} and relative velocity v_{rel}, where $d_{rel} = c\tau/2$ and $v_{rel} = \lambda_c f_D/2$, in which c is the speed of the light, τ is the time delay, f_D is the Doppler frequency. It is assumed that $f_c \gg B$ and $f_D \gg \Delta f$ such that f_D is a constant over the sub-carriers, while $\tau < T_g$ such that the inter-symbol interference is avoided.

The estimation of relative distance and speed in OFDM-radar can be transformed into a spectral estimation problem using periodogram algorithm [27], [31]. Utilizing the periodogram algorithm, the parameters of each ST can be estimated separately once the number of STs has been determined. Assuming that the parameters of different STs are distinguishable in the spectral estimation of the periodogram and are only affected by background interference and noise, we can focus on a typical ST for performance analysis. Along this

[3]Note that only inter-cell interference is retained since different CUs occupy different resource elements.

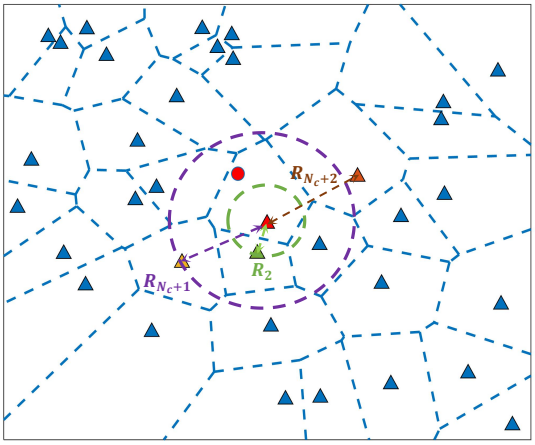

Figure 2: Framework of cooperative BF.

vein, the radar observation on the (m,n)-th resource element with respect to the typical ST is given by

$$[\boldsymbol{Y}_r]_{m,n} = \sqrt{P_t \mathcal{L}_1^r}\boldsymbol{f}_1^H(\theta_1)\underbrace{\boldsymbol{a}_r(\theta_1)\boldsymbol{a}_t^T(\theta_1)}_{\triangleq \boldsymbol{G}_1(\theta_1)}\boldsymbol{w}_1[\boldsymbol{S}_1]_{m,n}e^{j2\pi m T f_D} e^{-j2\pi n \Delta f \tau} + \underbrace{\sum_{i\in\Phi_B|1}\sqrt{P_t\mathcal{L}_{1,i}^c}\underbrace{\boldsymbol{f}_1^H(\theta_1)\boldsymbol{H}_{1,i}}_{\triangleq \boldsymbol{\nu}_{1,i}^H(\theta_1)}\boldsymbol{w}_i[\boldsymbol{S}_i]_{m,n}e^{-j2\pi n\Delta f\tau_{1,i}}}_{\text{inter-BS interference}} + [\boldsymbol{Z}_1]_{m,n}, \quad (2)$$

where $\mathcal{L}_1^r = \frac{\lambda_c^2 \xi}{(4\pi)^3 d_1^{-2\alpha_r}}$ is the amplitude attenuation factor, with ξ denoting the radar cross-section (RCS) of the ST and α_r denoting the pathloss exponent for the sensing channel. The vector $\boldsymbol{f}_1^H(\theta_1) \in \mathbb{C}^{1\times N_r}$ is the receive BF vector with θ_1 denoting the angel between the typical ST and BS 1. $\boldsymbol{a}_r(\theta_1) = [1,\cdots,e^{j\pi(N_r-1)\cos\theta_1}]^T \in \mathbb{C}^{N_r\times 1}$ and $\boldsymbol{a}_t(\theta_1) = [1,\cdots,e^{j\pi(N_t-1)\cos\theta_1}]^T \in \mathbb{C}^{N_t\times 1}$ are the receive and transmit steering vectors, respectively. $\mathcal{L}_{1,i}^c$ denotes the pathloss between the sensing interference BS i and the BS 1. $\boldsymbol{H}_{1,i} \in \mathbb{C}^{N_t\times N_r}$, with each entry distributed as $\mathcal{CN}(0,1)$, represents the interference channel matrix between the interference BS i and BS 1. $\boldsymbol{\nu}_{1,i}^H(\theta_1) = \boldsymbol{f}_1^H(\theta_1)\boldsymbol{H}_{1,i} \in \mathbb{C}^{1\times N_t}$ is the combined sensing interference channel between BS i and the typical BS 1 while sensing the typical ST 1. $[\boldsymbol{Z}_1]_{m,n} \sim \mathcal{CN}(0,\sigma_r^2)$ is the Gaussian noise. Note that $\boldsymbol{w}_1$ and $\boldsymbol{w}_i$ are the BF vectors that depend only on the quasi-static channel, thus the subscripts $[m,n]$ are omitted for statistical analysis. To avoid the influence of symbol $[\boldsymbol{S}_1]_{m,n}$ on sensing, the symbol-by-symbol phase rotations are applied and thus

$$\left[\widetilde{\boldsymbol{Y}}_r\right]_{m,n} = [\boldsymbol{Y}_r]_{m,n} / [\boldsymbol{S}_1]_{m,n} \quad (3)$$
$$= \sqrt{P_t\mathcal{L}_1^r}\boldsymbol{f}_1^H(\theta_1)\boldsymbol{G}_1(\theta_1)\boldsymbol{w}_1 e^{j2\pi m T f_D}e^{-j2\pi n\Delta f\tau} + \underbrace{\sum_{i\in\Phi_B|1}\sqrt{P_t\mathcal{L}_{1,i}^c}\boldsymbol{\nu}_{1,i}^H(\theta_1)\boldsymbol{w}_i\left[\widetilde{\boldsymbol{S}_i}\right]_{m,n}e^{-j2\pi n\Delta f\tau_{1,i}}}_{\text{inter-BS interference}} + \left[\widetilde{\boldsymbol{Z}}_1\right]_{m,n},$$

where $\widetilde{\boldsymbol{S}_i}$ and $\widetilde{\boldsymbol{Z}}_1$ are symbols and noise after phase rotation.

C. Cooperative BF Design

Since the sensing echo signal suffers from round-trip path loss compared to the severe interference signal that transmitted directly by other BSs, the cooperative BF is designed to mitigate the sensing interference from other BSs. On the transmitter side, a linear ZF BF strategy [32] is employed to gain spatial diversity while facilitating a tractable analysis. On the receiver-side, since the direction $\theta_{i,k}$ between the kth ST and ith BS can be estimated based on previous sensing results, the MRC BF vector can be designed as

$$\boldsymbol{f}_i^H(\theta_{i,k}) = \frac{1}{\sqrt{N_r}}[1,\cdots,e^{-j\pi(N_r-1)\cos\theta_{i,k}}] \in \mathbb{C}^{1\times N_r} \quad (4)$$

to maximize the sensing echo signal power. Since a linear combination of complex Gaussian RVs is still a complex Gaussian RV, the combined sensing interference channel vector $\boldsymbol{\nu}_{1,i}^H(\theta_1)$ still follows Rayleigh distribution. Therefore, similar to ZF BF in conventional multiuser communications, cooperative ZF BF can achieve sensing interference nulling by treating the combined sensing interference channels as the communication channels for other users within the same cell.

For instance, a nearest-neighbor cooperative BSs cluster of size N_c+1 centered on the typical BS (denoted be BS 1) is considered as illustrated in Fig. 2. The red point and triangle represent the typical CU and typical BS, respectively. The other BSs are indexed with the increasing distance between it and the BS 1. The green, yellow, and brown triangles represent the second, N_c+1th, and N_c+2th BS, respectively. To mitigate the severe sensing interference caused by the BS 1 on its N_c nearest BSs, the ZF BF of BS 1 will have to sacrifice KN_c degrees of freedom (DoF). Specifically, the collective combined sensing interference channel is denoted as

$$\boldsymbol{G}_I = \Big[\left(\boldsymbol{\nu}_{2,1}^H(\theta_1)\right)^T,\left(\boldsymbol{\nu}_{2,1}^H(\theta_2)\right)^T,\cdots,\left(\boldsymbol{\nu}_{2,1}^H(\theta_K)\right)^T,\cdots,\left(\boldsymbol{\nu}_{N_c+1,1}^H(\theta_1)\right)^T,\cdots,\left(\boldsymbol{\nu}_{N_c+1,1}^H(\theta_K)\right)^T\Big] \in \mathbb{C}^{N_t\times KN_c}. \quad (5)$$

Further, the normalized cooperative ZF BF matrix of BS 1 is given by

$$\boldsymbol{W}_1 = \frac{\widetilde{\boldsymbol{H}}_1^H\left(\widetilde{\boldsymbol{H}}_1\widetilde{\boldsymbol{H}}_1^H\right)^{-1}}{\left\|\widetilde{\boldsymbol{H}}_1^H\left(\widetilde{\boldsymbol{H}}_1\widetilde{\boldsymbol{H}}_1^H\right)^{-1}\right\|_2}, \quad (6)$$

where $\widetilde{\boldsymbol{H}}_1 = \left[\left(\boldsymbol{h}_1^H\right)^T,\boldsymbol{G}_I\right]^T$. Hence, the BF vector $\boldsymbol{w}_1$ of BS 1 can be extracted from the first column of matrix $\boldsymbol{W}_1$.

III. Communication Performance Evaluation

In this paper, we focus on the interference-limited networks, where noise is ignored due to severe interference in dense cell scenarios, and employ the signal-to-interference ratio (SIR) for performance analysis [33], [34]. Thus, according to (1),

the received communication SIR for the typical CU can be denoted as

$$\gamma_c = \frac{\mathcal{L}_1^c \left|\boldsymbol{h}_1^H \boldsymbol{w}_1\right|^2}{\sum_{i\in\Phi_B|1} \mathcal{L}_i^c \left|\boldsymbol{h}_i^H \boldsymbol{w}_i\right|^2} = \frac{\underbrace{d_1^{-\alpha_c}\left|\boldsymbol{h}_1^H \boldsymbol{w}_1\right|^2}_{\triangleq g_{cs}}}{\underbrace{\sum_{i\in\Phi_B|1} d_i^{-\alpha_c}\underbrace{\left|\boldsymbol{h}_i^H \boldsymbol{w}_i\right|^2}_{\triangleq g_{cI}}}_{\triangleq I_c}}, \quad (7)$$

where g_{cs} denotes the BF gain for the desired signal's communication channel, g_{cI} denotes the BF gain for the communication interference channel and I_c denotes the aggregated communication interference. ACCP and ACSE are adopted to evaluate and analyze communication performance.

A. Communication Performance Metrics

1) ACCP: For each CU, the CCP is defined as

$$\mathcal{P}_{ccov}(T_c) = \mathbb{P}\{\gamma_c > T_c\}, \quad (8)$$

where T_c is the required SIR beyond which the CU is regarded as covered. The ACCP represents the density of CUs covered by BSs, denoted by $\mathcal{P}_{accov}(T_c) = \lambda_B J \mathcal{P}_{ccov}(T_c)$.

2) ACSE: For each CU, the CSE is defined as

$$\mathcal{R}_c = \mathbb{E}\{\log_2(1+\gamma_c)\} \text{ (in bps)}, \quad (9)$$

which represents the average throughput. The ACSE represents the sum throughput per square kilometer, denoted by $\mathcal{R}_{ac} = \lambda_B J \mathcal{R}_c$.

B. Communication Performance Analysis

Note that each entry in channel vector $\boldsymbol{h}_i$ is a complex independent RV with distribution $\mathcal{CN}(0,1)$. Given the Rayleigh channel assumption, the communication channel gain distribution of the effective desired signal with N_t DoF is $g_{cs} = \left|\boldsymbol{h}_1^H \boldsymbol{w}_1\right|^2 \sim \Gamma(N_t, 1)$ [12]. To mitigate the severe sensing interference, the cooperative ZF BF has to sacrifice the KN_c DoF, so we have $g_{cs} \sim \Gamma(N_t - KN_c, 1)$. Since $\boldsymbol{h}_i^H$ is isotropic, when projected onto the subspace spanned by $\boldsymbol{w}_i$, the interference channel gain is distributed as $g_{cI} = \left|\boldsymbol{h}_i^H \boldsymbol{w}_i\right|^2 \sim \text{Exp}(1)$ [13].

To simplify the analysis, the effective channel gain g_{cs} can be further transformed as $\varpi_1 = \frac{g_{cs}}{N_t - KN_c}$, where $\varpi_1 \sim \Gamma\left(N_t - KN_c, \frac{1}{N_t - KN_c}\right)$ is a tractable distribution with a cumulative distribution function (CDF) of [35]

$$F_{\varpi_1}(x) = \mathbb{P}\{\varpi_1 < x\} = 1 - \sum_{m=0}^{m_1-1} \frac{(m_1 x)^m}{m!} e^{-m_1 x}, \quad (10)$$

with $m_1 = N_t - KN_c$ being a positive integer. The corresponding ACCP is given in the following theorem.

Theorem 1 (ACCP in Air-Ground Cooperative OFDM-ISAC Network): The downlink ACCP of air-ground cooperative OFDM-ISAC network is expressed as

$$\mathcal{P}_{accov}(T_c) = \lambda_B J \int_{r_1=0}^{\infty} \mathcal{P}_{ccov|R_1}(T_c, r_1) f_{R_1}(r_1)\, dr_1, \quad (11)$$

where $\mathcal{P}_{ccov|R_1}(T_c, r_1)$ denotes the conditional coverage probability, which is given by

$$\begin{aligned}\mathcal{P}_{ccov|R_1}(T_c, r_1) &\triangleq \mathbb{P}\{\gamma_c > T_c | R_1 = r_1\} \\ &= \sum_{m=0}^{m_1-1} \frac{(-\widehat{q}_1)^m}{m!} \frac{d^m}{d(\widehat{q}_1)^m} \mathcal{LT}_{I_c|R_1}(\widehat{q}_1),\end{aligned} \quad (12)$$

where $\widehat{q}_1 = \frac{T_c}{\mathcal{L}_1^c}$, $\mathcal{L}_1^c = \left(\frac{\lambda_c}{4\pi}\right)^2 \left(r_1^2 + \Delta h_c^2\right)^{-\frac{\alpha_c}{2}}$, $\Delta h_c = h_B - h_U$, $\mathcal{LT}_{I_c|R_1}(\widehat{q}_1)$ denotes the Laplace transform of the conditional aggregate interference $I_c|R_1$, and

$$f_{R_1}(r_1) = 2\pi\lambda_B r_1 e^{-\pi\lambda_B r_1^2} \quad (13)$$

denotes the probability density function (PDF) of ground serving distance [11].

Proof: See Appendix A.

Under the special case where $\alpha_c = 4$ and $N_c = (N_t - 1)/K$, the closed form of the CCP is given in the following proposition.

Proposition 1: (Closed Form of the ACCP) The ACCP under the special case of $\alpha_c = 4$ and $N_c = (N_t - 1)/K$ is expressed as

$$\mathcal{P}_{accov}(T_c) = \frac{\lambda_B J e^{-\pi\lambda_B \Delta h_c^2 T_c^{\frac{1}{2}} \arctan\sqrt{T_c}}}{T_c^{\frac{1}{2}} \arctan\sqrt{T_c} + 1}. \quad (14)$$

Proof: See Appendix B.

Remark 1: It can be observed that the CCP under the special case of $\alpha_c = 4$ and $N_c = (N_t - 1)/K$ is determined by the BS density λ_B, the vertical distance between the BS and the CU Δh_c, and the required SIR by CU T_c. Specifically, the ACCP decreases with the increasing Δh_c. Moreover, the ACCP first increases and then decreases with the increasing λ_B, where the maximum ACCP is achieved when $\lambda_B = \frac{1}{\pi \Delta h_c^2 T_c^{\frac{1}{2}} \arctan\sqrt{T_c}}$.

The corresponding ACSE is given in the following theorem.

Theorem 2 (ACSE in Air-Ground Cooperative OFDM-ISAC Network): The downlink ACSE of air-ground cooperative OFDM-ISAC network is expressed as

$$\mathcal{R}_{ac} = \lambda_B J \mathbb{E}\left\{\log_2(1+\gamma_c)\right\} = \frac{\lambda_B J}{\ln 2} \int_{t=0}^{\infty} \frac{\mathcal{P}_{ccov}(t)}{1+t}\, dt. \quad (15)$$

Proof: See Appendix C.

IV. Sensing Performance Evaluation

Given the radar sensing echos in (3), one can get the received SIR for the typical ST as

$$\begin{aligned}\gamma_r &= \frac{\mathcal{L}_1^r N_r \left|\boldsymbol{a}_t^T(\theta_1)\boldsymbol{w}_1\right|^2}{\sum_{i\in\Phi_B|\Phi_{CB}} \mathcal{L}_{1,i}^c \left|\boldsymbol{\nu}_{1,i}^H(\theta_1)\boldsymbol{w}_i\right|^2} \\ &= \frac{\xi d_1^{-2\alpha_r} N_r \underbrace{\left|\boldsymbol{a}_t^T(\theta_1)\boldsymbol{w}_1\right|^2}_{\triangleq g_{rs}}}{\underbrace{\sum_{i\in\Phi_B|\Phi_{CB}} 4\pi d_i^{-\alpha_c} \underbrace{\left|\boldsymbol{\nu}_{1,i}^H(\theta_1)\boldsymbol{w}_i\right|^2}_{\triangleq g_{rI}}}_{\triangleq I_r}},\end{aligned} \quad (16)$$

where $g_{rs} = \left|\boldsymbol{a}_t^T(\theta_1)\boldsymbol{w}_1\right|^2$ and $g_{rI} = \left|\boldsymbol{\nu}_{1,i}^H(\theta_1)\boldsymbol{w}_i\right|^2$ are the BF gains for the effective radar sensing channel and sensing

interference channel, respectively. I_r is the aggregate sensing interference. Φ_{CB} is the PPP of the cooperative BSs cluster. The radar sensing performance can be evaluated and analyzed from the perspectives of both coarse-grained detection tasks and fine-grained estimation tasks using different metrics, as described below.

A. Sensing Performance Metrics

1) ARDCP under CFAR: For each bin in the periodogram, the false alarm happens if $P_t I_r > \eta$ with η denoting the threshold. Therefore, the CFAR for each bin is defined as

$$\mathcal{P}_{CFAR,bin} = \mathbb{P}\{P_t I_r > \eta\}. \tag{17}$$

The corresponding CFAR during the CPI of an OFDM frame can be expressed as

$$\mathcal{P}_{CFAR,frame} = 1 - (1 - \mathcal{P}_{CFAR,bin})^{NM}. \tag{18}$$

Given the required CFAR $\mathcal{P}_{CFAR,frame}$, the threshold η can be recovered from (17) and (18). The corresponding required SIR can be further obtained as $T_r = \frac{\eta}{P_t I_r}$. The corresponding ARDCP under given CFAR can be defined as

$$\mathcal{P}_{arcov} = \lambda_B K \mathbb{P}\{NM\gamma_r > T_r\}, \tag{19}$$

which represents the density of detected STs by BSs that satisfies certain CFAR level, where NM comes from the signal processing gain of periodogram [36].

2) ACRB: Calculating the CRB for the entire OFDM signal, which consists of M symbols over N subcarriers, is highly complicated. The high complexity arises from the matrix $\boldsymbol{Y}_r$, where each entry has a different, random and unknown initial phase, due to the unknown Doppler frequency and the unknown time delay. Thus, by applying the ACRB over the entire resource blocks as described in [31], the estimation errors of $\widehat{d}_{rel}$ and $\widehat{v}_{rel}$ can be lower-bounded by

$$\text{var}(\widehat{d}_{rel}) \geqslant \mathcal{ACRB}(\widehat{d}_{rel}) = \frac{6}{\gamma_r (N^2-1) NM} \left(\frac{c}{4\pi \Delta f}\right)^2, \tag{20a}$$

$$\text{var}(\widehat{v}_{rel}) \geqslant \mathcal{ACRB}(\widehat{v}_{rel}) = \frac{6}{(M^2-1) MN\gamma_r} \left(\frac{c}{4\pi T f_c}\right)^2. \tag{20b}$$

B. Sensing Performance Analysis

To analyze the sensing performance, two useful lemmas are introduced as follows.

Lemma 1 (Gamma 2nd Order Moment Match [12]): Consider a RV X with expectation $\rho = \mathbb{E}\{X\}$, $\rho^{(2)} = \mathbb{E}\{X^2\}$, and variance $\varrho = \rho^{(2)} - \rho^2$. Then a Gamma approximation of X can be obtained by applying the 2nd-order moment match as $X \sim \Gamma(\alpha, \beta)$, where

$$\alpha = \rho^2/\varrho \text{ and } \beta = \varrho/\rho \tag{21}$$

are its shape and scale parameters, respectively.

Lemma 2 (Expectations with Isotropic Random Vectors [12]): Suppose that $\boldsymbol{w}_1$ is an $N_t \times 1$ isotropic random vector and $\boldsymbol{a}_t^T(\theta_1)$ is a constant vector. Then, we have

$$\rho_{|\boldsymbol{a}_t^T(\theta_1)} := \mathbb{E}_{\boldsymbol{w}_1}\left\{\left|\boldsymbol{a}_t^T(\theta_1)\boldsymbol{w}_1\right|^2\right\} = \frac{\boldsymbol{a}_t^H(\theta_1)\boldsymbol{a}_t(\theta_1)}{N_t}, \tag{22a}$$

$$\varrho_{|\boldsymbol{a}_t^T(\theta_1)} := \text{Var}_{\boldsymbol{w}_1}\left\{\left|\boldsymbol{a}_t^T(\theta_1)\boldsymbol{w}_1\right|^2\right\} = \frac{N_t - 1}{N_t + 1}\rho^2_{|\boldsymbol{a}_t^T(\theta_1)}. \tag{22b}$$

Based on Lemma 1 and Lemma 2, and following the assumptions in [12], the BF vector $\boldsymbol{w}_1$ is considered as an isotropic random vector with the distribution of the BF gain given in the following proposition.

Proposition 2 (Distribution of BF Gain): Suppose that $\boldsymbol{a}_t^T(\theta_1)$ is the phase-wise steering vector and $\boldsymbol{w}_1$ is an $N_t \times 1$ isotropic random vector, the distribution of BF gain for the effective radar sensing channel can be approximated as $g_{rs} \sim \Gamma\left(\frac{N_t+1}{N_t-1}, \frac{N_t-1}{N_t+1}\right)$.

Proof: See Appendix D.

For tractability, we further approximate $g_{rs} \sim \text{Exp}(1)$ when N_t is sufficiently large. Since the combined sensing channel vector $\boldsymbol{\nu}_{1,i}^H(\theta_1)$ remains Rayleigh distributed, the BF gain of the sensing interference channel follows the distribution $g_{rI} \sim \text{Exp}(1)$. The corresponding RDCP under CFAR is given in the following theorem.

Theorem 3 (ARDCP under CFAR in Air-Ground Cooperative OFDM-ISAC Network): The approximated ARDCP under CFAR of air-ground cooperative OFDM-ISAC network is expressed as

$$\mathcal{P}_{arcov} = \lambda_B K \int_{r_1=0}^{\infty} \mathcal{P}_{rcov|R_1}(T_r, r_1) f_{R_1}(r_1)\, dr_1, \tag{23}$$

where $\mathcal{P}_{rcov|R_1}(T_r, r_1)$ denotes the conditional coverage probability for radar sensing, which is given by

$$\begin{aligned}\mathcal{P}_{rcov|R_1}(T_r, r_1) &\triangleq \mathbb{P}\{NM\gamma_r > T_r | R_1 = r_1\} \\ &= \mathcal{LT}_{I_r|R_1}(q_2),\end{aligned} \tag{24}$$

where $q_2 = \frac{T_r}{NMN_r\mathcal{L}_1^r}$, $\mathcal{LT}_{I_r|R_1}(q_2)$ denotes the Laplace transform of the conditional aggregated interference $I_r|R_1$, and $f_{R_1}(r_1)$ denotes the pdf of ground serving distance during sensing.

Proof: See Appendix E.

To simplify the analysis and facilitate the derivation of the distribution of the aggregate sensing interference, we approximate the aggregated sensing interference by only considering the strongest interferer, which is a common approach in radar sensing literatures [37], [38]. The corresponding relationship between the minimum SIR and required CFAR for radar detection is given in the following proposition.

Proposition 3 (The Strongest Interferer Approximation): Under the strongest interferer approximation, the explicit relationship between the minimum SIR and required CFAR for radar detection is expressed as

$$T_r = -\ln\left[1 - (1 - \mathcal{P}_{CFAR,frame})^{\frac{1}{NM}}\right]. \tag{25}$$

Proof: See Appendix F.

The approximation that considers only the strongest interference source, while ignoring interference from more distant BSs, is generally accurate when the interference from the nearest BS is significantly greater than that from distant BSs. The corresponding ACRBs are given in the following theorem.

Table I: Simulation Parameter Settings

Symbol	Value	Parameter Description
N_t	10	Number of transmit antennas
N_r	10	Number of receive antennas
λ_B	10 BSs/Km^2	Density of BSs
J	4 CUs/BS	Number of CUs served by each BS
K	3 STs/BS	Number of STs sensed by each BS
N_c	3	Number of cooperative BSs
h_B	50 m	Height of BS
h_U	1.5 m	Height of CU
h_T	100 m	Height of ST
f_c	5.89 GHz	Carrier frequency
B	10 MHz	Bandwidth
M	50	Number of OFDM symbols per frame
N	64	Number of subcarriers
T	8 μs	Symbol duration
α_c	4	Pathloss exponent of the communication channel
α_r	2	Pathloss exponent of the sensing channel
ξ	1 m^2	RCS of ST
d_{rel}	20 m	Relative distance of ST
v_{rel}	80 km/h	Relative speed of ST

Theorem 4 (Approximated ACRB in Air-Ground Cooperative OFDM-ISAC Network): The approximated ACRBs of estimated $\widehat{d}$ and $\widehat{v}$ in air-ground cooperative OFDM-ISAC network are expressed as

$$\overline{\mathcal{ACRB}}\left(\widehat{d}_{rel}\right) = \mathbb{E}_{\gamma_r}\left\{\frac{6}{(N^2-1)NM\gamma_r}\left(\frac{c}{4\pi\Delta f}\right)^2\right\} = \frac{6}{(N^2-1)\mathcal{I}_r^0}\left(\frac{c}{4\pi\Delta f}\right)^2, \tag{26a}$$

$$\overline{\mathcal{ACRB}}\left(\widehat{v}_{rel}\right) = \mathbb{E}_{\gamma_r}\left\{\frac{6}{\gamma_r(M^2-1)MM}\left(\frac{c}{4\pi T f_c}\right)^2\right\} = \frac{6}{(M^2-1)\mathcal{I}_r^0}\left(\frac{c}{4\pi T f_c}\right)^2, \tag{26b}$$

where $\mathcal{I}_r^0 = \int_{t=0}^{\infty} \mathcal{P}_{rcov}(t)\, dt$.

Proof: See Appendix G.

V. Simulation Results

In this section, simulations are conducted to illustrate the C&S performances in the cooperative OFDM-ISAC networks. The theoretical analysis is validated through Monte Carlo simulations. Subsequently, the C&S performances under different system parameters are further demonstrated. The simulation parameters according to IEEE 802.11p [39] are listed in Table I unless specified otherwise.

A. Communication Performance

Fig. 3 illustrates the effects of the required SIR, BS height, and BS density on ACCP. The simulation results are closely aligned with the analytical results, validating the accuracy of Theorem 1. It can be observed that the ACCP decreases with the increasing required SIR since increasing the required SIR by CU makes it harder to be covered. It can also be observed that the ACCP decreases with the increasing BS height. This is because increasing BS heights results in longer distance between the BS and CU and thus higher propagation path loss of signals. Since the ground distance between the interfering BS and CU r_i is longer than that between the serving BS and CU r_1, increasing the BS heights leads to lower SIR. Moreover, one can observe that at high BS height,

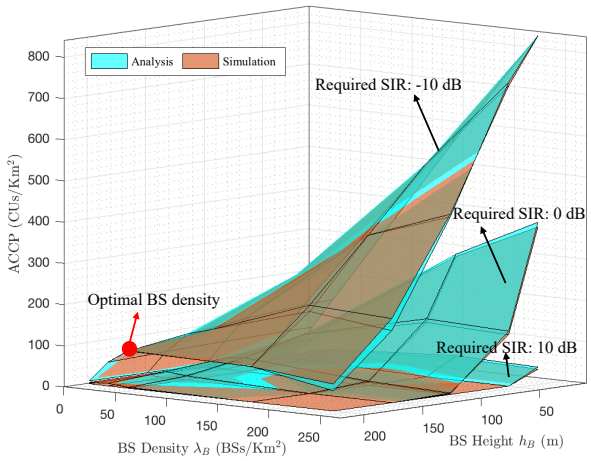

Figure 3: Effects of the required SIR, BS density and height on ACCP.

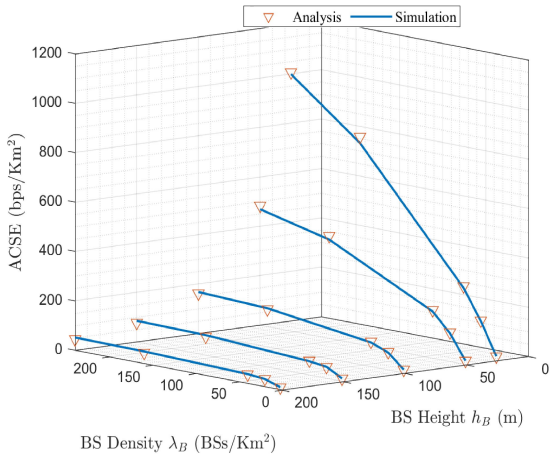

Figure 4: Effects of BS density and height on ACSE.

the ACCP first increases but then decreases with the increasing BS density, which indicates that there exists an optimal BS density for maximizing the ACCP.

Fig. 4 illustrates the effects of BS density and height on ACSE. The simulation results are closely aligned with the analytical results, validating the accuracy of Theorem 2. It can be observed the ACSE decreases with the increasing BS height, since increasing the BS height results in lower SIR. Moreover, the ACSE increases with the increasing BS density, as more BSs can provide more communication resource.

In addition, the HPPP model-based analysis is further compared with the lattice model-based and actual BS deployments, where the BS density is $\lambda_B = 9$ BSs/Km^2 based on the actual BS deployments in a city. As shown in Fig. 5, the performance of HPPP model is worse than the actual BS deployment, while the performance of lattice model is better than the actual BS deployment. The HPPP model-based analysis is meaningful to guide the deployment of air-ground OFDM-ISAC networks by providing a performance lower bound on the actual BS deployment.

B. Sensing Performance

Fig. 6 illustrates the effects of number of OFDM subcarriers and symbols on the ARDCP under different CFAR requirements. The simulation results are closely aligned with

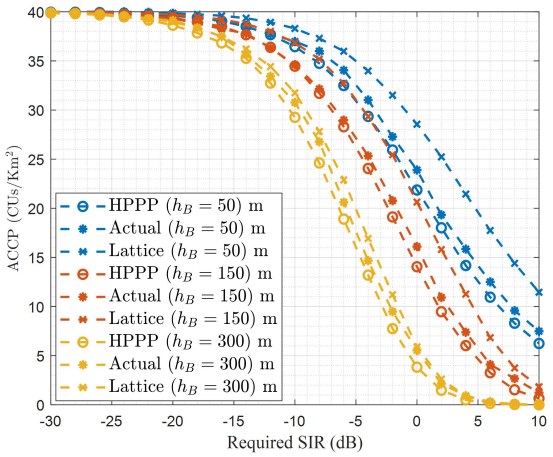

Figure 5: ACCP comparisons among HPPP, actual and lattice models.

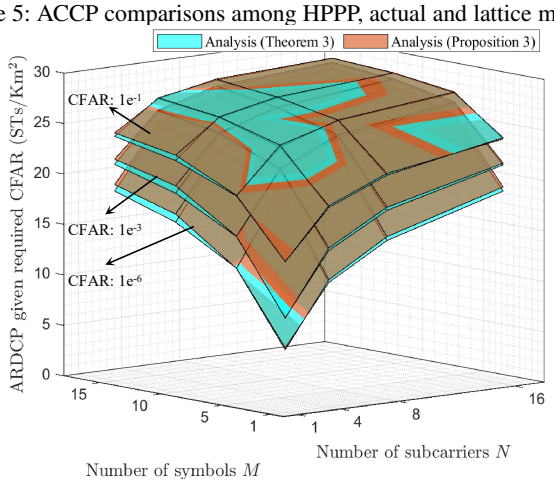

Figure 6: Effects of numbers of OFDM subcarriers and symbols on the ARDCP under different CFAR requirements.

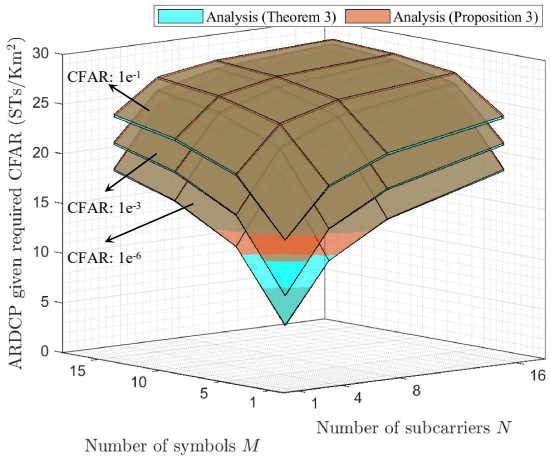

Figure 7: ARDCP derived in Theorem 3 and approximated ARDCP by Proposition 3.

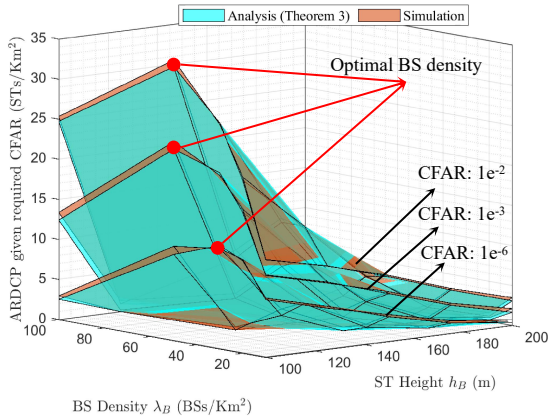

Figure 8: Effects of BS density and ST height on ARDCP.

the analytical results, validating the accuracy of Theorem 3. It can be observed that the ARDCP under all CFAR settings increases with the increasing number of symbols M and subcarriers N. This is due to the increment of signal processing gain in the periodogram. Moreover, the ARDCP decreases with the decreasing required CFAR, since lower required CFAR results in higher required SIR that is harder to be satisfied.

Fig. 7 illustrates the ARDCP derived in Theorem 3 and approximated ARDCP according to Proposition 3. It can be observed that the approximated ARDCP is closely aligned with the ARDCP derived in Theorem 3 and thus can serve as a reasonable close approximation.

The effects of BS density and ST height on ARDCP are illustrated in Fig. 8. The simulation results are closely aligned with both the ARDCP derived in Theorem 3 and the approximated ARDCP according to Proposition 3. It can be observed that ARDCP decreases with the increasing ST height, since increasing ST height results in longer distance between the BS and ST, which leads to lower SIR. Moreover, the ARDCP first increases but then decreases with the increasing BS density, which indicates that there exists an optimal BS density for maximizing the ARDCP.

Fig. 9 illustrates the effects of number of OFDM subcarriers and symbols, and ST height on the approximated ACRBs of both distance and speed estimations. The simulation results are closely aligned with the analytical results, validating the accuracy of Theorem 4. It can be observed that the ACRBs of both distance and speed estimations decrease with the increasing number of OFDM subcarriers and symbols, which demonstrates the benefit brought by larger number of OFDM symbols and/or subcarriers. Specifically, the ACRB of distance estimation is mainly affected by the number of subcarriers, whereas the ACRB of speed estimation is mainly affected by the number of symbols, which are consistent with Theorem 4. It can also be observed that the ACRBs of both distance and speed estimations increase with the increasing ST height, since increasing ST height results in longer distance and thus larger estimation errors.

Fig. 10 illustrates the effects of BS height on the C&S performances, where the height of ST is set as $h_T = 300$ m. It can be observed that increasing BS height results in decreasing ACCP and increasing ARDCP given required CFAR, which indicates that the ARDCP can be improved with the reduction of ACCP. It can also be observed that increasing BS height results in decreasing ACSE as well as decreasing approximate ACRBs of distance and speed, which indicates that the sensing accuracy can be improved by sacrificing the communication efficiency. The above results demonstrate the tradeoff between C&S performances.

Fig. 11 illustrates the effects of BS density on the C&S performances. It can be observed that both the ACCP and

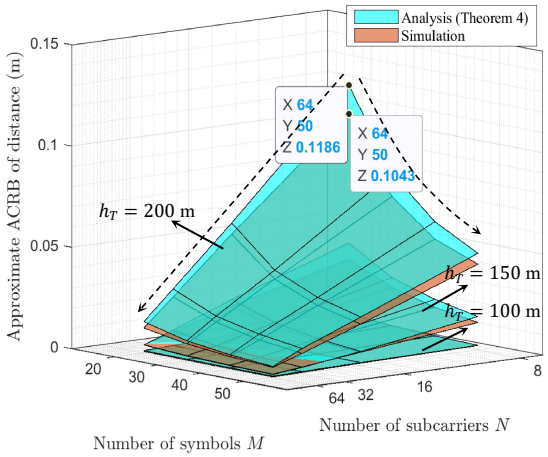

(a) Approximate ACRB of distance

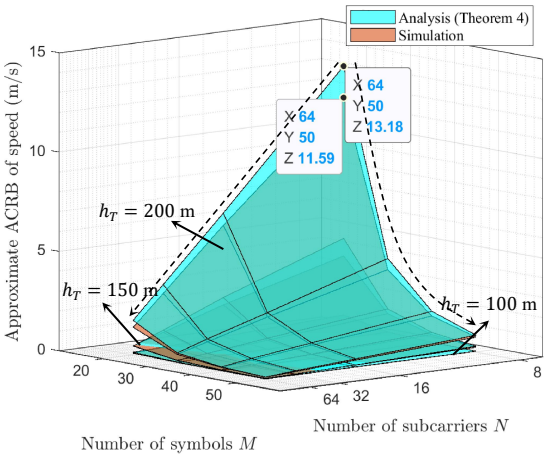

(b) Approximate ACRB of speed

Figure 9: The approximate ACRBs with different numbers of subcarriers N and symbols M.

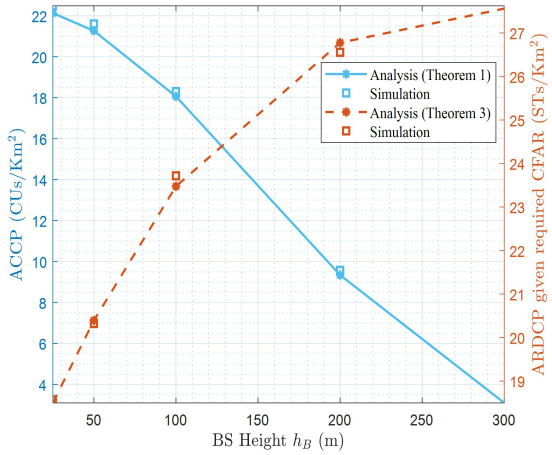

(a) Tradeoff between ACCP and ARDCP.

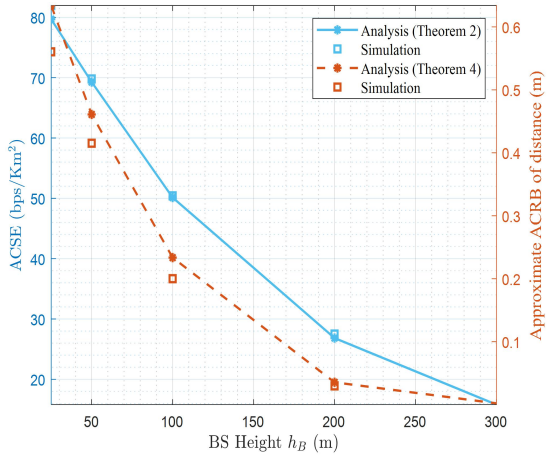

(b) Tradeoff between ACSE and approximate ACRB of distance.

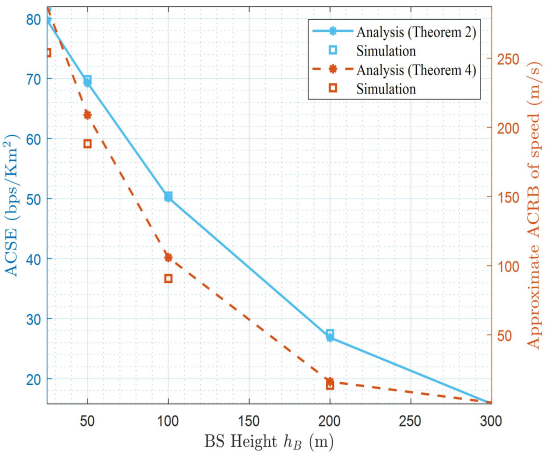

(c) Tradeoff between ACSE and approximate ACRB of speed.

Figure 10: C&S tradeoff with respect to BS height.

the ARDCP given required CFAR are first increasing and then decreasing with the increasing BS density. However, the optimal BS density for maximizing the ARDCP is different from that for maximizing the ACCP. Moreover, the optimal BS density for maximizing the ACCP increases with the lower required SIR, while the optimal BS density for maximizing the ARDCP increases with the higher required CFAR.

VI. Conclusion

This paper introduces a generalized air-ground cooperative OFDM-ISAC network for network-level C&S performance analysis based on SG. The cooperative BF strategies are designed to mitigate the interference between ISAC BSs. The C&S performance is further analyzed with respect to different metrics including ACCP, ACSE, ARDPC, and ACRB. For communication, the effects of system parameters such as BS density and height on ACCP and ACSE are analyzed. A closed form of ACCP is further provided under the special case where the pathloss exponent is equal to 4. For sensing, the effects of system parameters such as the number of OFDM subcarriers and symbols on ARDPC and ACRB are analyzed. Simulation results are presented to validate the theoretical analysis and illustrate the effects of system parameters on the network performance. It is observed that increasing the BS height results in better sensing performance but worse communication performance, which indicates that there exists a tradeoff between C&S performances. Moreover, both the ACCP and ARDCP first increase and then decrease with the increasing BS density, while the maximum ACCP or ARDCP is achieved at different BS densities. The sensing performance can be further improved by increasing the numbers of OFDM subcarriers and symbols, or decreasing the ST height. This

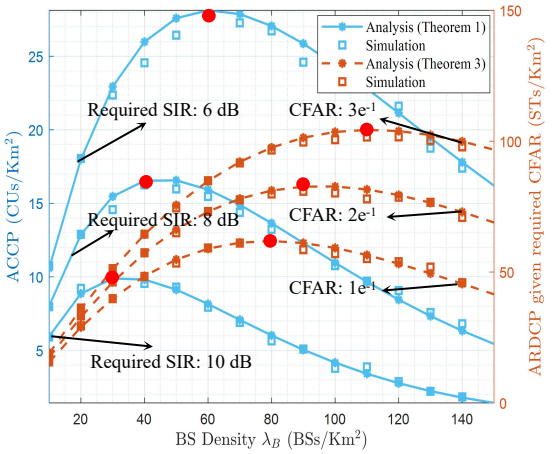

Figure 11: C&S tradeoff with respect to BS density.

paper contributes to the promising new area of air-ground cooperative wireless networks for ISAC by providing a solid network-level performance analysis framework, while many interesting follow-up research issues warrant further investigation, such as the scenarios of millimeter-wave signals, bi-static sensing, aerial CUs, and so on.

Appendix A
Proof of Theorem 1

Given a ground serving distance R_1, the conditional CCP can be calculated as

$$\begin{aligned}\mathcal{P}_{ccov|R_1}(T_c, r_1) &\triangleq \mathbb{P}\left\{\gamma_c > T_c | R_1 = r_1\right\} \\ &= \mathbb{E}_{I_c}\left\{\mathbb{P}\left\{\varpi_1 > \underbrace{\frac{T_c}{m_1 \mathcal{L}_1^c}}_{\triangleq q_1} I_c | R_1 = r_1\right\}\right\} \\ &\overset{(a)}{=} \sum_{m=0}^{m_1-1} \frac{\overbrace{(m_1 q_1)^m}^{\triangleq \widehat{q}_1}}{m!} \mathbb{E}_{I_c}\left\{I_c^m e^{-\widehat{q}_1 I_c} | R_1 = r_1\right\} \\ &\overset{(b)}{=} \sum_{m=0}^{m_1-1} \frac{(-\widehat{q}_1)^m}{m!} \frac{d^m}{d(\widehat{q}_1)^m} \mathcal{LT}_{I_c|R_1}(\widehat{q}_1),\end{aligned} \tag{27}$$

where (a) comes from (10) and (b) comes from that $\mathcal{LT}_{I_c|R_1}(\widehat{q}_1) = \mathbb{E}_{I_c}\left\{e^{-\widehat{q}_1 I_c} | R_1 = r_1\right\}$, which is the Laplace transform of the conditional aggregate interference $I_c|R_1$ evaluated at $\widehat{q}_1$ for the communication serving BS 1.

Further, the Laplace transform of $I_c|R_1$ can be derived as

$$\begin{aligned}\mathcal{LT}_{I_c|R_1}(\widehat{q}_1) &= \mathbb{E}_{I_c}\left\{e^{-\widehat{q}_1 I_c} | R_1 = r_1\right\} \\ &= \mathbb{E}_{\Phi_B, g_{cI}}\left\{e^{-\widehat{q}_1 \sum_{i\in\Phi_B|1} \mathcal{L}_i^c g_{cI}}\right\} \\ &= \mathbb{E}_{\Phi_B}\left\{\prod_{i\in\Phi_B|1} \mathbb{E}_{g_{cI}}\left\{e^{-\widehat{q}_1 \mathcal{L}_I^c g_{cI}}\right\}\right\} \\ &\overset{(a)}{=} \mathbb{E}_{\Phi_B}\left\{\prod_{i\in\Phi_B|1} \underbrace{(1+\widehat{q}_1\mathcal{L}_I^c)^{-1}}_{\triangleq \mathcal{M}_{g_{cI}}(\widehat{q}_1)}\right\} \\ &\overset{(b)}{=} e^{-\lambda_B \underbrace{\int_{\mathbf{x}\in\mathbb{R}^2} [1-\mathcal{M}_{g_{cI}}(\widehat{q}_1)]\, d\mathbf{x}}_{\triangleq \mathcal{I}_c(\widehat{q}_1)}},\end{aligned} \tag{28}$$

where $\mathcal{L}_I^c = \left(\frac{\lambda_c}{4\pi}\right)^2 (r_I^2 + \Delta h_c^2)^{-\frac{\alpha_c}{2}}$, (a) comes from the moment generating function (MGF) of the exponential distribution $X \sim \text{Exp}(\lambda)$ [40], i.e.,

$$\mathcal{M}_X(t) = \mathbb{E}_X\left\{e^{tX}\right\} = \left(1 - t\lambda^{-1}\right)^{-1}, \tag{29}$$

and (b) comes from the probability generating functional (PGF) of the HPPP of BSs [40], i.e.,

$$\mathbb{E}_{\Phi_B}\left\{\prod_{i\in\Phi_B|1} \mathcal{M}_{g_{cI}}(\widehat{q}_1)\right\} = e^{-\lambda_B \int_{\mathbf{x}\in\mathbb{R}^2}\left[1-\mathcal{M}_{g_{cI}}(\widehat{q}_1)\right] d\mathbf{x}}. \tag{30}$$

Therefore, the above integral $\mathcal{I}_c(\widehat{q}_1)$ can be processed as

$$\begin{aligned}\mathcal{I}_c(\widehat{q}_1) &\triangleq \int_{\mathbf{x}\in\mathbb{R}^2} [1-\mathcal{M}_{g_{cI}}(\widehat{q}_1)]\, d\mathbf{x} \\ &= 2\pi \int_{r_I > r_1} \left[1 - (1+\widehat{q}_1\mathcal{L}_I^c)^{-1}\right] r_I\, dr_I \\ &= 2\pi \int_{r_I > r_1} \left\{1 - \left[1 + T_c\left(\frac{r_1^2+\Delta h_c^2}{r_I^2+\Delta h_c^2}\right)^{\frac{\alpha_c}{2}}\right]^{-1}\right\} r_I\, dr_I \\ &= \pi \int_{x > r_1^2+\Delta h_c^2} \left\{1 - \left[1 + \frac{\underbrace{T_c\left(r_1^2+\Delta h_c^2\right)^{\frac{\alpha_c}{2}}}_{\triangleq \widetilde{q}_1}}{x^{\frac{\alpha_c}{2}}}\right]^{-1}\right\} dx \\ &= \pi \int_{x > r_1^2+\Delta h_c^2} \frac{\widetilde{q}_1 x^{-\frac{\alpha_c}{2}}}{1+\widetilde{q}_1 x^{-\frac{\alpha_c}{2}}}\, dx \\ &= \frac{2\pi}{\alpha_c}\widetilde{q}_1 \int_{t>0}^{\left(r_1^2+\Delta h_c^2\right)^{-\frac{\alpha_c}{2}}} \frac{t^{-\frac{2}{\alpha_c}}}{1+\widetilde{q}_1 t}\, dt \\ &\overset{(a)}{=} \frac{2\pi}{\alpha_c - 2} T_c^{1-\frac{2}{\alpha_c}} \left(\frac{\lambda_c}{4\pi}\right)^{\frac{4}{\alpha_c}} \widehat{q}_1^{\frac{2}{\alpha_c}}\, {}_2F_1\left(1, 1-\frac{2}{\alpha_c}; 2-\frac{2}{\alpha_c}; -T_c\right),\end{aligned} \tag{31}$$

where (a) comes from

$$\int_0^u \frac{x^{\mu-1}}{(1+\beta x)^\nu}\, dx = \frac{u^\mu}{\mu}\, {}_2F_1\left(\nu, \mu; 1+\mu; -\beta u\right), \tag{32}$$

in which ${}_2F_1(a, b; c; z) = F(a, b; c; z)$ denotes the Gauss hypergeometric function [41].

To obtain $\frac{d^m}{d(\widehat{q}_1)^m}\mathcal{LT}_{I_c|R_1}(\widehat{q}_1)$, the derivatives of a composite exponential function in the form $F\left(f(x)\right) = e^{-a\cdot f(x)}$ is further studied. Through mathematical induction, one can show that

$$F^{(m)}\left(\cdot\right) = \binom{m-1}{0}F^{(m-1)}\left(\cdot\right)\left[-af^{(1)}(x)\right] + \cdots + \binom{m-1}{m-2}F^{(1)}\left(\cdot\right)\left[-af^{(m-1)}(x)\right] + \binom{m-1}{m-1}F\left(\cdot\right)\left[-af^{(m)}(x)\right]. \quad (33)$$

From (31), we derive

$$\frac{d^m}{d(\widehat{q}_1)^m}\mathcal{I}_c(\widehat{q}_1) = \frac{2\pi}{\alpha_c - 2}T_c^{1-\frac{2}{\alpha_c}}\left(\frac{\lambda_c}{4\pi}\right)^{\frac{4}{\alpha_c}}\left[\frac{2}{\alpha_c}\left(\frac{2}{\alpha_c}-1\right)\cdots\left(\frac{2}{\alpha_c}-m+1\right)\right]\widehat{q}_1^{\frac{2}{\alpha_c}-m}\,{}_2F_1\left(1,1-\frac{2}{\alpha_c};2-\frac{2}{\alpha_c};-T_c\right). \quad (34)$$

Further, $\frac{d^m}{d(\widehat{q}_1)^m}\mathcal{LT}_{I_c|R_1}(\widehat{q}_1)$ in (27) can be obtained from (33) and (34) by recursion.

Appendix B
Proof of Proposition 1

When $\alpha_c = 4$, (31) can be rewritten as

$$\begin{aligned}&\mathcal{I}_c(\widehat{q}_1)\\ &= \frac{2\pi}{\alpha_c - 2}T_c^{1-\frac{2}{\alpha_c}}\left(\frac{\lambda_c}{4\pi}\right)^{\frac{4}{\alpha_c}}\widehat{q}_1^{\frac{2}{\alpha_c}}\,{}_2F_1\left(1,1-\frac{2}{\alpha_c};2-\frac{2}{\alpha_c};-T_c\right)\\ &\overset{(a)}{=} \pi T_c^{\frac{1}{2}}\arctan\sqrt{T_c}(r_1^2+\Delta h_c^2),\end{aligned} \quad (35)$$

where (a) comes from the simple form of the Gauss hypergeometric function at $\delta = 1/2$, which is given by [42]

$${}_2F_1\left(1,\delta;\delta+1;-z\right) = \frac{\arctan\sqrt{z}}{\sqrt{z}}. \quad (36)$$

Further, the CCP can be re-expressed as

$$\begin{aligned}&\mathcal{P}_{ccov}(T_c)\\ &= \int_{r_1=0}^{\infty} e^{-\pi\lambda_B T_c^{\frac{1}{2}}\arctan\sqrt{T_c}(r_1^2+\Delta h_c^2)}2\pi\lambda_B r_1 e^{-\pi\lambda_B r_1^2}\,dr_1\\ &= \pi\lambda_B e^{-\pi\lambda_B\Delta h_c^2 T_c^{\frac{1}{2}}\arctan\sqrt{T_c}}\int_{x=0}^{\infty} e^{-\pi\lambda_B(T_c^{\frac{1}{2}}\arctan\sqrt{T_c}+1)x}dx\\ &= \frac{e^{-\pi\lambda_B\Delta h_c^2 T_c^{\frac{1}{2}}\arctan\sqrt{T_c}}}{T_c^{\frac{1}{2}}\arctan\sqrt{T_c}+1}.\end{aligned} \quad (37)$$

Appendix C
Proof of Theorem 2

The CSE of a typical CU defined in (9) can be obtained as

$$\begin{aligned}&\mathcal{R}_c = \mathbb{E}\left\{\log_2\left(1+\gamma_c\right)\right\}\\ &= \int_{r_1=0}^{\infty}\mathbb{E}\left\{\log_2\left[1+\gamma_c\left(r_1\right)\right]\right\}\ f_{R_1}(r_1)\,dr_1\\ &= \int_{r_1=0}^{\infty}\int_{T_c=0}^{\infty}\mathbb{P}\left\{\log_2[1+\gamma_c(r_1)] > T_c|R_1=r_1\right\}dT_c\ f_{R_1}(r_1)dr_1\\ &= \int_{r_1=0}^{\infty}\int_{T_c=0}^{\infty}\mathbb{P}\left\{\ln[1+\gamma_c(r_1)] > \ln 2T_c|R_1=r_1\right\}dT_c\ f_{R_1}(r_1)dr_1\\ &= \int_{r_1=0}^{\infty}\int_{T_c=0}^{\infty}\mathbb{P}\left\{\varpi_1 > \frac{(2^{T_c}-1)}{m_1\mathcal{L}_1^c}I_c|R_1=r_1\right\}dT_c\ f_{R_1}(r_1)dr_1\\ &= \int_{r_1=0}^{\infty}\int_{t=0}^{\infty}\underbrace{\mathbb{P}\left\{\varpi_1 > \frac{t}{m_1\mathcal{L}_1^c}I_c|R_1=r_1\right\}}_{=\mathcal{P}_{ccov|R_1}(t,r_1)}\frac{dt}{1+t}\ f_{R_1}(r_1)dr_1\\ &= \frac{1}{\ln 2}\int_{t=0}^{\infty}\frac{\mathcal{P}_{ccov|R_1}(t,r_1)f_{R_1}(r_1)}{1+t}\,dr_1\,dt\\ &\overset{(a)}{=} \frac{1}{\ln 2}\int_{t=0}^{\infty}\frac{\mathcal{P}_{ccov}(t)}{1+t}\,dt,\end{aligned} \quad (38)$$

where (a) comes from Theorem 1.

Appendix D
Proof of Proposition 2

First, we take the expectation of the conditional terms in Lemma 2 to remove the conditioning on $\boldsymbol{a}_t^T(\theta_1)$ for the case where $\boldsymbol{a}_t^T(\theta_1)$ is the phase-wise steering vector. Then, we can show

$$\rho := \mathbb{E}_{\boldsymbol{w}_1,\boldsymbol{a}_t^T(\theta_1)}\left\{\left|\boldsymbol{a}_t^T(\theta_1)\boldsymbol{w}_1\right|^2\right\} = 1, \quad (39a)$$

$$\varrho := \mathrm{Var}_{\boldsymbol{w}_1,\boldsymbol{a}_t^T(\theta_1)}\left\{\left|\boldsymbol{a}_t^T(\theta_1)\boldsymbol{w}_1\right|^2\right\} = \frac{N_t-1}{N_t+1}. \quad (39b)$$

Next, we obtain that g_{rs} is distributed as a Gamma RV with $\alpha_{g_{rs}} = \frac{N_t+1}{N_t-1}$ and $\beta_{g_{rs}} = \frac{N_t-1}{N_t+1}$ using the Gamma approximation in Lemma 1.

Appendix E
Proof of Theorem 3

Due to the cooperative BF on the transmitter side, for a cooperative BS cluster of size N_c+1, the ground interference distance between the central BS 1 and the interfered BS should satisfy $r_I \geq r_{N_c+2}$, where r_{N_c+2} denotes the ground distance between BS 1 and the (N_c+2)-th BS (i.e., the closest interfered BS). Further, the ground interference distance can be approximated by taking the expected value of r_{N_c+2} as

$$\begin{aligned}\overline{r}_{N_c+2} &= \int_0^{\infty} r_{N_c+2}f_{R_{N_c+2}}(r_{N_c+2})\,dr_{N_c+2}\\ &\overset{(a)}{=} \int_0^{\infty} r_{N_c+2}\frac{2\lambda_B\pi r_{N_c+2}\left(\lambda_B\pi r_{N_c+2}^2\right)^{N_c}}{(N_c)!}e^{-\lambda_B\pi r_{N_c+2}^2}\,dr_{N_c+2}\\ &= \int_0^{\infty}\frac{x^{N_c+0.5}}{\sqrt{\lambda_B\pi}\,(N_c)!}e^{-x}\,dx\\ &\overset{(b)}{=} \frac{\Gamma(N_c+1.5)}{\sqrt{\lambda_B\pi}\,(N_c)!},\end{aligned} \quad (40)$$

where (a) comes from the pdf of r_{N_c+2} [40], which can be written as

$$f_{R_{N_c+2}}(r_{N_c+2}) = \frac{2\lambda_B\pi r_{N_c+2}\left(\lambda_B\pi r_{N_c+2}^2\right)^{N_c}}{(N_c)!}e^{-\lambda_B\pi r_{N_c+2}^2}, \quad (41)$$

and (b) comes from the standard Gamma function $\Gamma(x) = \int_0^{\infty} t^{x-1}e^{-t}\,dt$.

To analyze the RDCP under CFAR, it is essential to establish a link between the CFAR $\mathcal{P}_{CFAR,frame}$ and the detection threshold T_r. This requires determining the distribution of the aggregate sensing interference. Therefore, we first formulate

the characteristic function (CF) of the aggregate sensing interference as

$$\begin{aligned}
&\varphi_{I_r}(-\omega) = \mathbb{E}_{I_r}\left\{e^{-\jmath\omega I_r}\right\} \\
&= \mathbb{E}_{I_r}\left\{e^{-\jmath\omega\sum_{i\in\Phi_B|\Phi_{CB}}\mathcal{L}^c_{1,i}\left|\boldsymbol{\nu}^H_{1,i}(\theta_1)\boldsymbol{w}_i\right|^2}\right\} \\
&= \mathbb{E}_{\Phi_B}\left\{\mathbb{E}_{g_{rI}}\left\{e^{-\jmath\omega\sum_{i\in\Phi_B|\Phi_{CB}}\mathcal{L}^c_I g_{rI}}\right\}\right\} \\
&= \mathbb{E}_{\Phi_B}\left\{\prod_{i\in\Phi_B|\Phi_{CB}}\mathbb{E}_{g_{rI}}\left\{e^{-\jmath\omega\mathcal{L}^c_I g_{rI}}\right\}\right\} \\
&= \mathbb{E}_{\Phi_B}\left\{\prod_{i\in\Phi_B|\Phi_{CB}}(1+\jmath\omega\mathcal{L}^c_I)^{-1}\right\} \\
&\approx e^{-\lambda_B\pi\int_{x>\overline{r}^2_{N_c+2}}\left\{1-\left[1+\jmath\omega\left(\frac{\lambda_c}{4\pi}\right)^2 x^{-\frac{\alpha_c}{2}}\right]^{-1}\right\}dx}.
\end{aligned} \tag{42}$$

Further, the CDF of aggregate sensing interference can be obtained by utilizing the Gil-Pelaez's inversion theorem [43], i.e.,

$$F_{I_r}(x) = \frac{1}{2} - \frac{1}{\pi}\int_0^\infty \frac{1}{\omega}\Im\left[\varphi_{I_r}(-\omega)e^{\jmath\omega x}\right]\,d\omega. \tag{43}$$

Thus, the CFAR of any bin in periodogram can be expressed as

$$\mathcal{P}_{CFAR,bin} \triangleq \mathbb{P}\left\{P_t I_r > \eta\right\} = 1 - F_{I_r}\left(\eta/P_t\right). \tag{44}$$

In theory, given the tolerable CFAR, we can get the corresponding FA detection threshold η and thus T_r. Hence, given a ground serving distance R_1, the conditional RDCP under CFAR can be expressed as

$$\begin{aligned}
&\mathcal{P}_{rcov|R_1}(T_r, r_1) \triangleq \mathbb{P}\left\{NM\gamma_r > T_r | R_1 = r_1\right\} \\
&= \mathbb{P}\left\{g_{rs} > \underbrace{\frac{T_r}{NMN_r\mathcal{L}^r_1}}_{\triangleq q_2} I_r | R_1 = r_1\right\} \\
&\overset{(a)}{\approx} \mathbb{E}_{I_r}\left\{e^{-q_2 I_r}|R_1 = r_1\right\} \\
&= \mathcal{LT}_{I_r|R_1}(q_2),
\end{aligned} \tag{45}$$

where (a) comes from the CDF of an approximate exponential distribution.

Further, the Laplace transform of $I_r|R_1$ can be derived as

$$\begin{aligned}
\mathcal{LT}_{I_r|R_1}(q_2) &= \mathbb{E}_{I_r}\left\{e^{-q_2 I_r}|R_1 = r_1\right\} \\
&= \mathbb{E}_{\Phi_B, g_{rI}}\left\{e^{-q_2\sum_{i\in\Phi_B|\Phi_{CB}}\mathcal{L}^c_{1,i}g_{rI}}\right\} \\
&= \mathbb{E}_{\Phi_B}\left\{\prod_{i\in\Phi_B|\Phi_{CB}}\mathbb{E}_{g_{rI}}\left\{e^{-q_2\mathcal{L}^c_I g_{rI}}\right\}\right\} \\
&\overset{(a)}{=} \mathbb{E}_{\Phi_B}\left\{\prod_{i\in\Phi_B|\Phi_{CB}}\underbrace{(1+q_2\mathcal{L}^c_I)^{-1}}_{\triangleq\mathcal{M}_{g_{rI}}(q_2)}\right\} \\
&= e^{-\lambda_B\underbrace{\int_{\mathbf{x}\in\mathbb{R}^2}\left[1-\mathcal{M}_{g_{rI}}(q_2)\right]\,d\mathbf{x}}_{\triangleq\mathcal{I}_r(q_2)}},
\end{aligned} \tag{46}$$

where $\mathcal{L}^c_I = \left(\frac{\lambda_c}{4\pi}\right)^2 r_I^{-\alpha_c}$ and (a) comes from the MGF of the exponential distribution.

Then, the above integral $\mathcal{I}_r(q_2)$ can be further expressed as

$$\begin{aligned}
\mathcal{I}_r(q_2) &\triangleq \int_{\mathbf{x}\in\mathbb{R}^2}\left[1-\mathcal{M}_{g_{rI}}(q_2)\right]\,d\mathbf{x} \\
&= 2\pi\int_{r_I>\overline{r}_{N_c+2}}\left\{1-\left[1+\underbrace{\frac{4\pi T_r\left(r_1^2+\Delta h_r^2\right)^{\alpha_r}}{NMN_r\xi}}_{\triangleq\widehat{q}_2}r_I^{-\alpha_c}\right]^{-1}\right\}r_I dr_I \\
&= \frac{2\pi}{\alpha_c}\int_0^{\overline{r}^{-\alpha_c}_{N_c+2}}\frac{\widehat{q}_2 x^{-\frac{2}{\alpha_c}}}{1+\widehat{q}_2 x}\,dx \\
&\overset{(a)}{=} \frac{2\pi\overline{r}^{2-\alpha_c}_{N_c+2}}{\alpha_c-2}\,{}_2F_1\left(1, 1-\frac{2}{\alpha_c}; 2-\frac{2}{\alpha_c}; -\widehat{q}_2\overline{r}^{-\alpha_c}_{N_c+2}\right),
\end{aligned} \tag{47}$$

where (a) comes from (32).

Appendix F
Proof of Proposition 3

Specifically, we assume that the (N_c+2)-th BS is the nearest BS causing interference on the typical BS with the ground distance of $r_I = \overline{r}_{N_c+1}$. Consequently, we can obtain that

$$I_r = \mathcal{L}_{1,N_c+2}g_{rI} \approx \left(\frac{\lambda_c}{4\pi}\right)^2\overline{r}^{-\alpha_c}_{N_c+1}g_{rI}. \tag{48}$$

Thus, the CFAR of any bin in periodogram can be expressed as

$$\begin{aligned}
\mathcal{P}_{CFAR,bin} &\triangleq \mathbb{P}\left\{P_t I_r > \eta\right\} \\
&= 1 - F_{I_r}\left(\frac{\eta}{P_t\left(\frac{\lambda_c}{4\pi}\right)^2\overline{r}^{-\alpha_c}_{N_c+1}}\right) \\
&\overset{(a)}{=} e^{-\underbrace{\frac{\eta}{P_t\left(\frac{\lambda_c}{4\pi}\right)^2\overline{r}^{-\alpha_c}_{N_c+1}}}_{\triangleq q_3}},
\end{aligned} \tag{49}$$

where (a) comes from the exponential CDF of g_{rI}. Further, given the CFAR $\mathcal{P}_{CFAR,frame}$, we can have

$$\begin{aligned}
\eta &= -q_3\ln\mathcal{P}_{CFAR,bin} \\
&= -q_3\ln\left[1-\left(1-\mathcal{P}_{CFAR,frame}\right)^{\frac{1}{NM}}\right]
\end{aligned} \tag{50}$$

and

$$T_r = -\ln\left[1-\left(1-\mathcal{P}_{CFAR,frame}\right)^{\frac{1}{NM}}\right]. \tag{51}$$

Appendix G
Proof of Theorem 4

The expectation of radar sensing SIR can be expressed as

$$\begin{aligned}
&\mathbb{E}\left\{\gamma_r\right\} = \int_{r_1=0}^\infty\mathbb{E}\left\{\gamma_r\left(r_1\right)\right\}f_{R_1}(r_1)\,dr_1 \\
&= \int_{r_1=0}^\infty\int_{T_c=0}^\infty\mathbb{P}\left\{\gamma_r(r_1) > T_r|R_1 = r_1\right\}\,dT_r\;f_{R_1}(r_1)\,dr_1 \\
&= \frac{1}{NM}\int_{t=0}^\infty\int_{r_1=0}^\infty\mathcal{P}_{rcov|R_1}(t, r_1)\;f_{R_1}(r_1)\,dr_1\,dt
\end{aligned}$$

$$\overset{(a)}{=} \frac{1}{NM} \underbrace{\int_{t=0}^{\infty} \mathcal{P}_{rcov}(t)\, dt}_{\triangleq \mathcal{I}_r^0}, \tag{52}$$

where (a) comes from Theorem 3.

Therefore, the approximated ACRBs can be obtained as

$$\begin{aligned}\overline{\mathcal{ACRB}}\left(\widehat{d}_{rel}\right) &= \mathbb{E}_{\gamma_r}\left\{\frac{6}{(N^2-1)NM\gamma_r}\left(\frac{c}{4\pi\Delta f}\right)^2\right\} \\ &= \frac{6}{(N^2-1)\mathcal{I}_r^0}\left(\frac{c}{4\pi\Delta f}\right)^2, \end{aligned} \tag{53a}$$

$$\begin{aligned}\overline{\mathcal{ACRB}}\left(\widehat{v}_{rel}\right) &= \frac{6}{(M^2-1)MN\gamma_r}\left(\frac{c}{4\pi T f_c}\right)^2 \\ &= \frac{6}{(M^2-1)\mathcal{I}_r^0}\left(\frac{c}{4\pi T f_c}\right)^2. \end{aligned} \tag{53b}$$

REFERENCES

[1] F. Liu, Y. Cui, C. Masouros, J. Xu, T. X. Han, Y. C. Eldar, and S. Buzzi, "Integrated sensing and communications: Toward dual-functional wireless networks for 6G and beyond," *IEEE J. Sel. Areas Commun.*, vol. 40, no. 6, pp. 1728–1767, 2022.

[2] Y. Cui, F. Liu, X. Jing, and J. Mu, "Integrating sensing and communications for ubiquitous IoT: Applications, trends, and challenges," *IEEE Netw.*, vol. 35, no. 5, pp. 158–167, 2021.

[3] X. Li, Y. Gong, K. Huang, and Z. Niu, "Over-the-air integrated sensing, communication, and computation in IoT networks," *IEEE Wireless Commun.*, vol. 30, no. 1, pp. 32–38, 2023.

[4] X. Li, F. Liu, Z. Zhou, G. Zhu, S. Wang, K. Huang, and Y. Gong, "Integrated sensing, communication, and computation over-the-air: MIMO beamforming design," *IEEE Trans. Wireless Commun.*, vol. 22, no. 8, pp. 5383–5398, 2023.

[5] G. Zhu, Z. Lyu, X. Jiao, P. Liu, M. Chen, J. Xu, S. Cui, and P. Zhang, "Pushing AI to wireless network edge: An overview on integrated sensing, communication, and computation towards 6G," *Sci. China Inf. Sci.*, vol. 66, no. 3, pp. 130 301:1–19, 2023.

[6] D. Wen, P. Liu, G. Zhu, Y. Shi, J. Xu, Y. C. Eldar, and S. Cui, "Task-oriented sensing, computation, and communication integration for multi-device edge AI," *IEEE Trans. Wireless Commun.*, vol. 23, no. 3, pp. 2486 – 2502, 2024.

[7] "Introduction to 6G | IMT-2030," [Online]. Avaliabled: https://www.tonex.com/training-courses/introduction-to-6g-imt-2030/, Apr. 2020.

[8] F. Liu, C. Masouros, A. P. Petropulu, H. Griffiths, and L. Hanzo, "Joint radar and communication design: Applications, state-of-the-art, and the road ahead," *IEEE Trans. Commun.*, vol. 68, no. 6, pp. 3834–3862, 2020.

[9] J. A. Zhang, F. Liu, C. Masouros, R. W. Heath, Z. Feng, L. Zheng, and A. Petropulu, "An overview of signal processing techniques for joint communication and radar sensing," *IEEE J. Sel. Topics Signal Process.*, vol. 15, no. 6, pp. 1295–1315, 2021.

[10] M. Haenggi, *Stochastic geometry for wireless networks*. Cambridge, U.K.: Cambridge Univ. Press, 2012.

[11] J. G. Andrews, F. Baccelli, and R. K. Ganti, "A tractable approach to coverage and rate in cellular networks," *IEEE Trans. Commun.*, vol. 59, no. 11, pp. 3122–3134, 2011.

[12] R. W. Heath Jr, T. Wu, Y. H. Kwon, and A. C. Soong, "Multiuser MIMO in distributed antenna systems with out-of-cell interference," *IEEE Trans. Signal Process.*, vol. 59, no. 10, pp. 4885–4899, 2011.

[13] K. Hosseini, W. Yu, and R. S. Adve, "A stochastic analysis of network MIMO systems," *IEEE Trans. Signal Process.*, vol. 64, no. 16, pp. 4113–4126, 2016.

[14] K. Han, K. Huang, and R. W. Heath, "Connectivity and blockage effects in millimeter-wave air-to-everything networks," *IEEE Wireless Commun. Lett.*, vol. 8, no. 2, pp. 388–391, 2018.

[15] M. Braun, R. Tanbourgi, and F. K. Jondral, "Co-channel interference limitations of OFDM communication-radar networks," *EURASIP J. Wireless Commun. Netw.*, vol. 2013, no. 207, pp. 1–16, 2013.

[16] A. Al-Hourani, R. J. Evans, S. Kandeepan, B. Moran, and H. Eltom, "Stochastic geometry methods for modeling automotive radar interference," *IEEE Trans. Intell. Transp. Syst.*, vol. 19, no. 2, pp. 333–344, 2017.

[17] Y. Wang, Q. Zhang, Z. Wei, Y. Lin, and Z. Feng, "Performance analysis of coordinated interference mitigation approach for automotive radar," *IEEE Internet Things J.*, vol. 10, no. 13, pp. 11 683–11 695, 2023.

[18] P. Ren, A. Munari, and M. Petrova, "Performance tradeoffs of joint radar-communication networks," *IEEE Wireless Commun. Lett.*, vol. 8, no. 1, pp. 165–168, 2018.

[19] Z. Sun, S. Yan, N. Jiang, J. Zhou, and M. Peng, "Performance analysis of integrated sensing and communication networks with blockage effects," *arXiv preprint arXiv:2403.18621*, 2024.

[20] N. R. Olson, J. G. Andrews, and R. W. Heath, "Coverage and rate of joint communication and parameter estimation in wireless networks," *IEEE Trans. Inf. Theory*, vol. 70, no. 1, pp. 206–243, 2023.

[21] X. Gan, C. Huang, Z. Yang, X. Chen, J. He, Z. Zhang, C. Yuen, Y. L. Guan, and M. Debbah, "Performance tradeoffs of joint radar-communication networks," *IEEE J. Sel. Areas Commun.*, early access, 2024.

[22] A. Salem, K. Meng, C. Masouros, F. Liu, and D. López-Pérez, "Rethinking dense cells for integrated sensing and communications: A stochastic geometric view," *IEEE Open J. Commun. Soc.*, vol. 5, pp. 2226–2239, 2024.

[23] K. Meng, C. Masouros, G. Chen, and F. Liu, "Network-level integrated sensing and communication: Interference management and bs coordination using stochastic geometry," *arXiv preprint arXiv:2311.09052*, 2023.

[24] K. Meng, C. Masouros, A. P. Petropulu, and L. Hanzo, "Cooperative ISAC Networks: Performance Analysis, Scaling Laws and Optimization," *arXiv preprint arXiv:2404.14514*, 2024.

[25] Y. Jiang, X. Li, G. Zhu, H. Li, J. Deng, and Q. Shi, "6G non-terrestrial networks enabled low-altitude economy: Opportunities and challenges," *arXiv preprint arXiv:2311.09047*, 2023.

[26] Z. Fei, X. Wang, N. Wu, J. Huang, and J. A. Zhang, "Air-ground integrated sensing and communications: Opportunities and challenges," *IEEE Commun. Mag.*, vol. 61, no. 5, pp. 55–61, 2023.

[27] C. Sturm and W. Wiesbeck, "Waveform design and signal processing aspects for fusion of wireless communications and radar sensing," *Proc. of the IEEE*, vol. 99, no. 7, pp. 1236–1259, 2011.

[28] X. Lin, L. Jiang, and J. G. Andrews, "Performance analysis of asynchronous multicarrier wireless networks," *IEEE Trans. Commun.*, vol. 63, no. 9, pp. 3377–3390, 2015.

[29] A. Ali, R. Vesilo, and M. Di Renzo, "Stochastic geometry analysis of multi-user asynchronous OFDM wireless networks," *IEEE Wireless Commun. Lett.*, vol. 8, no. 3, pp. 845–848, 2019.

[30] R. Schmidt, "Multiple emitter location and signal parameter estimation," *IEEE Trans. Antennas Propag.*, vol. 34, no. 3, pp. 276–280, 1986.

[31] M. Braun, "OFDM radar algorithms in mobile communication networks," *Ph.D. Thesis at Karlsruher Institute of Technology*, 2014.

[32] T. Yoo and A. Goldsmith, "On the optimality of multiantenna broadcast scheduling using zero-forcing beamforming," *IEEE J. Sel. Areas Commun.*, vol. 24, no. 3, pp. 528–541, 2006.

[33] R. Schmidt, "Spectral efficiency of dynamic coordinated beamforming: A stochastic geometry approach," *IEEE Trans. Wireless Commun.*, vol. 14, no. 1, pp. 230–241, 2014.

[34] J. Park, N. Lee, J. G. Andrews, and R. W. Heath, "On the optimal feedback rate in interference-limited multi-antenna cellular systems," *IEEE Trans. Wireless Commun.*, vol. 15, no. 8, pp. 5748–5762, 2016.

[35] C. Forbes, M. Evans, N. Hastings, and B. Peacock, *Statistical distributions*. Hoboken, NJ, USA: John Wiley & Sons, 2011.

[36] C. Sturm, E. Pancera, T. Zwick, and W. Wiesbeck, "A novel approach to OFDM radar processing," in *Proc. IEEE Radar Conf.*, 2009, pp. 1–4.

[37] A. Munari, L. Simić, and M. Petrova, "Stochastic geometry interference analysis of radar network performance," *IEEE Commun. Lett.*, vol. 22, no. 11, pp. 2362–2365, 2018.

[38] K. V. Mishra, B. S. MR, and B. Ottersten, "Stochastic-geometry-Based interference modeling in automotive radars using matern hard-core process," in *Proc. IEEE Radar Conf.*, 2020, pp. 1–5.

[39] D. H. Nguyen and R. W. Heath, "Delay and Doppler processing for multi-target detection with IEEE 802.11 OFDM signaling," in *Proc. IEEE ICASSP*, 2017, pp. 3414–3418.

[40] D. Stoyan, W. S. Kendall, and J. Mecke, *Stochastic Geometry and Its Applications*. New York, NY, USA: Wiley, 1995.

[41] I. S. Gradshteyn and I. M. Ryzhik, *Table of Integrals, Series, and Products*. New York, NY, USA: Academic Press, 2007.

[42] M. Haenggi, "Meta distributions—Part 2: Properties and interpretations," *IEEE Commun. Lett.*, vol. 25, no. 7, pp. 2094–2098, 2021.

[43] J. Gil-Pelaez, "Note on the inversion theorem," *Biometrika*, vol. 38, no. 3-4, pp. 481–482, 1951.